



# Self-delivery photodynamic-hypoxia alleviating nanomedicine synergizes with anti-PD-L1 for cancer immunotherapy

Xianquan Feng<sup>a,b,1</sup>, Zhenzhen Chen<sup>b,1</sup>, Zhihong Liu<sup>b</sup>, Xiaoling Fu<sup>a</sup>, Hongtao Song<sup>a,b,\*</sup>, Qian Zhang<sup>a,\*</sup>

<sup>a</sup> The School of Pharmacy, Fujian Medical University, Fuzhou 350108, PR China

<sup>b</sup> Fuzong Clinical Medical College of Fujian Medical University, Fuzhou 350025, PR China

## ARTICLE INFO

### Keywords:

Hypoxic microenvironment  
Immunogenetic cell death  
Anti-PD-L1 therapy  
Tumor-associated macrophages  
Cancer immunotherapy

## ABSTRACT

The low level of T-lymphocyte infiltration in tumor is a key issue in cancer immunotherapy. Stimulating anti-tumor immune responses and improving the tumor microenvironment are essential for enhancing anti-PD-L1 immunotherapy. Herein, atovaquone (ATO), protoporphyrin IX (PpIX), and stabilizer (ATO/PpIX NPs) were constructed to self-assemble with hydrophobic interaction and passively targeted to tumor for the first time. The studies have indicated that PpIX-mediated photodynamic induction of immunogenic cell death combined with relieving tumor hypoxia by ATO, leading to maturation of dendritic cells, polarization of M2-type tumor-associated macrophages (TAMs) towards M1-type TAMs, infiltration of cytotoxic T lymphocytes, reduction of regulatory T cells, release of pro-inflammatory cytokines, resulting in an effective anti-tumor immune response synergized with anti-PD-L1 against primary tumor and pulmonary metastasis. Taken together, the combined nanoplatform may be a promising strategy to enhance cancer immunotherapy.

## 1. Introduction

Malignant tumors seriously threaten public health and impose a heavy economic burden on society (Xia et al., 2022). For malignancies prone to distal metastases, therapies that block the PD-1/PD-L1 signaling pathway are promising for its rapid and durable clearance of tumor cells, which has attracted much attention for clinical efficacy in a wide range of tumor types (Villacampa et al., 2022). However, difficulties remain due to the “cold” property of malignancies, with low cytotoxic T lymphocyte infiltration, a high proportion of M2-type tumor-associated macrophages (TAMs) and an immunosuppressive microenvironment, which are the key factors leading to the failure of tumor immunotherapy (Anderson et al., 2017; Yang et al., 2020; Zhao et al., 2019). To date, the treatment of malignant tumors remains extremely challenging.

Compared with conventional chemotherapy and radiotherapy, inducing immunogenetic cell death (ICD), which in turn releases tumor-associated antigens (TAA) to enhance tumor immunogenicity, is a promising strategy for transforming “cold” tumors into “hot” tumors (Jiao et al., 2021; Yang et al., 2023). When ICD occurs in cells,

calreticulin (CRT) by the endoplasmic reticulum to cell membrane surface is activated to send “eat me” signals to antigen-presenting cells (APC), while immunogenic substances like high mobility group box 1 (HMGB1) and adenosine triphosphate (ATP) are released to send “find me” signals to APC, inducing the maturation and differentiation of APC and leading to an anti-tumor immune cascade (Aaes and Vandenabeele, 2021; Li et al., 2021b). Recent studies have shown that a marginally invasive local surgery of photodynamic therapy (PDT) is few side effects and high selectivity, which is suitable for the treatment of various solid tumors with the help of fiber optic, endoscopic and other interventional techniques (Im et al., 2021). PDT triggers an ICD cascade response, thereby increasing tumor sensitivity to immunotherapy as a means of immune stimulation (Choi et al., 2022; Li et al., 2022b). The photosensitizer of protoporphyrin IX (PpIX) is an FDA approved metabolite of 5-aminoketovaleic acid and has a excellent biosafety due to its endogenous photosensitization (He et al., 2022). However, photosensitizer is hydrophobic and lacks tumor targeting, and the PDT efficacy is limited by the oxygen at the tumor site (Zhang et al., 2018).

Compared to normal tissues, solid tumors have a large number of hypoxic areas due to inadequate oxygen supply caused by the

\* Corresponding authors at: The School of Pharmacy, Fujian Medical University, Fuzhou 350108, PR China (H.S.).

E-mail addresses: [sohoto@vip.163.com](mailto:sohoto@vip.163.com) (H. Song), [1009467948@qq.com](mailto:1009467948@qq.com) (Q. Zhang).

<sup>1</sup> These authors contributed equally to this paper.

incomplete function of the tumor vascular system and rapid cell proliferation (Liao et al., 2023). Evidences suggest that intra-tumor hypoxia increases tumor aggressiveness and resistance to chemotherapy and radiotherapy (Li et al., 2021a; Shahpouri et al., 2022). The hypoxic microenvironment created by solid tumors leads to ineffectiveness of PDT results and limits the efficacy of immunotherapy. Recent evidences suggest that a hypoxic tumor microenvironment promotes the polarization of immune-supportive M1-type TAMs to immunosuppressive M2-type TAMs, which in turn hinders the immune response to tumors (Bai et al., 2022; Rodell et al., 2018). Studies have shown that M2-type TAMs could induce T cell functional exhaustion (Le et al., 2018). Normalization of tumor hypoxia could reverse the polarization of M2-type TAMs, generating a intense immune response against tumor proliferation (Ruffell and Coussens, 2015). Reducing mitochondrial oxygen consumption is a more effective way to alleviate tumor hypoxia than increasing oxygen supply (Secomb et al., 1995). Recent studies have shown that the clinical anti-malarial drug atovaquone (ATO) affects the function of mitochondrial respiratory chain complex III, decreasing endogenous oxygen consumption and ultimately alleviating the hypoxic immunosuppressive microenvironment (Ashton et al., 2016).

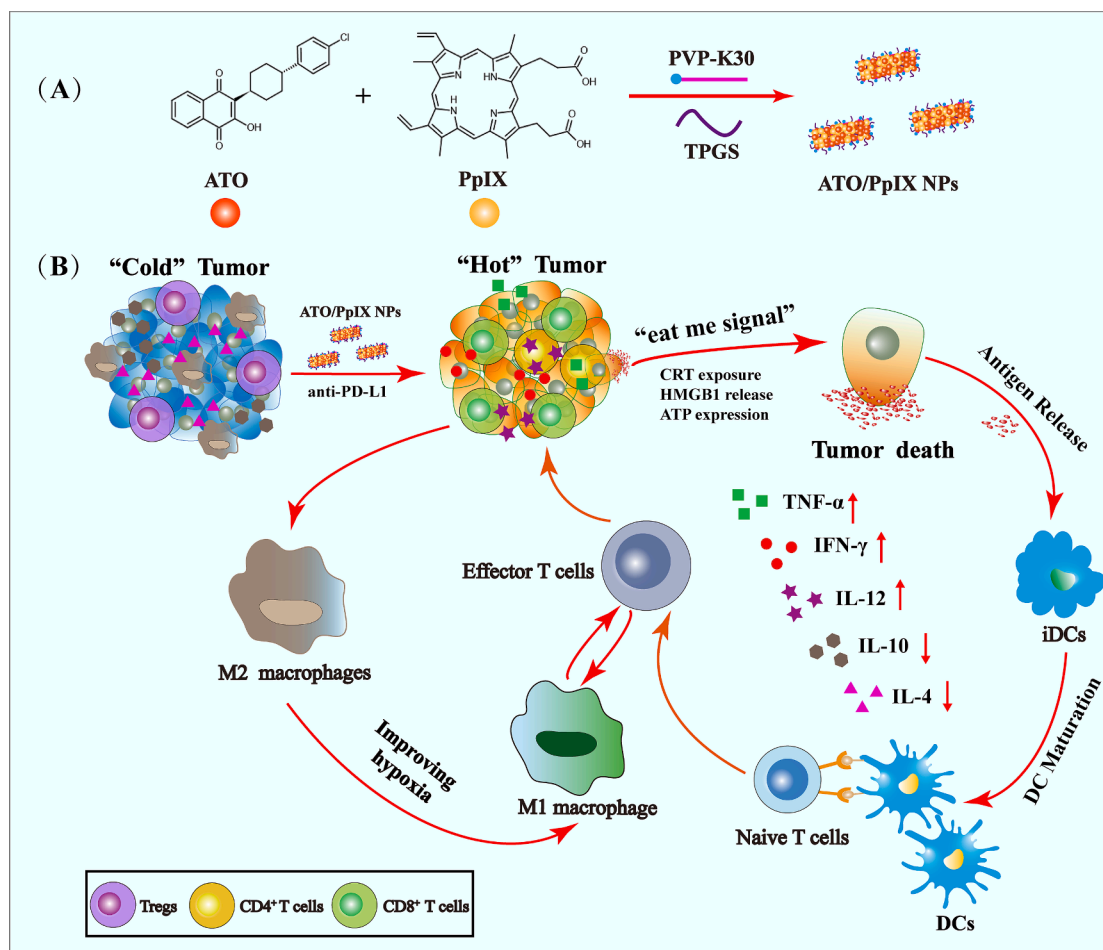
Therefore, a well-constructed drug delivery platform is needed to synergistically improve the tumor hypoxic microenvironment, induce ICD and M2-type TAMs exhaustion, which will ultimately increase tumor tissue T lymphocyte infiltration. As shown in the Scheme 1, ATO/PpIX NPs were constructed by self-assembly of ATO, PpIX and stabilizers through intermolecular interaction forces. ATO/PpIX NPs passively targeted tumor tissue through EPR effects, releasing ATO to improve the hypoxic microenvironment, enhancing PpIX-mediated PDT-induced

ICD, releasing TAA to induce maturation of dendritic cells, while improving the hypoxic microenvironment by ATO also induced M2-type TAMs polarization toward M1-type TAMs. The above strategy transformed “cold tumor” into “hot tumor”, synergized with anti-PD-L1 immunotherapy, inhibited the proliferation of tumors both primary tumor and pulmonary metastasis, ultimately achieving a synergistic effect of the photodynamic-alleviating hypoxic-immunotherapy.

## 2. Materials and methods

### 2.1. Materials

Atovaquone, Protoporphyrin IX, D- $\alpha$ -Tocopherol polyethylene glycol 1000 succinate (TPGS), Polyvinylpyrrolidone K30 (PVP-K30) were obtained from Sigma-Aldrich (USA). RPMI 1640 medium with penicillin-streptomycin, phosphate buffered saline (PBS), and the Calcein-AM/Propidium Iodide (PI) Staining Kit were obtained from KeyGEN BioTECH Co., Ltd (China). Fetal Bovine Serum (FBS) was obtained from Gibco (USA). PD-L1 monoclonal antibody was obtained from Bio X Cell (USA). CD8, and Tregs monoclonal antibody were purchased from Wuhan Saiville Biotechnology Co., Ltd (China). The monoclonal antibody of CD11c-FITC, CD45-PerCP-Cy5.5, CD44L-PE-Cy7, CD80-PE, CD86-APC, CD3-PE, CD11b-FITC, CD206-Alexa 647, CD8-FITC, CD11c-PE-Cy7, and F4/80-PE were obtained from BD Biosciences (USA). The monoclonal antibody of MHC-II-PE-Cy7, CD62L-BV421 were obtained from Biologend (USA).



**Scheme 1.** (A) The preparation procedure of the ATO/PpIX NPs. (B) Schematic illustration of ATO/PpIX NPs plus laser coupled with anti-PD-L1 induces cancer immunotherapy through immunogenic cell death effect, alleviating hypoxia, and PD-1/PD-L1 blockade.

## 2.2. Cells and animals

CT-26 cells (murine colon cancer) and 4T1 cells (murine breast cancer) were incubated in RPMI 1640 medium with penicillin–streptomycin with 10 % FBS.

Balb/c mice (female, 18–20 g) were purchased from Animal Center, Fuzong Clinical College of Fujian Medical University. For establishing CT-26 murine colon cancer and 4T1 metastatic breast cancer models, the  $1 \times 10^6$  CT-26 cells/100  $\mu$ L or  $1 \times 10^6$  4T1 cells/100  $\mu$ L were subcutaneously inoculated into the right armpit of mice, respectively. Once the tumor volume attained about 50–100 mm<sup>3</sup>, the mice were applied to different experiments. All animal experiments were performed based on the guidelines of the Institutional Animal Care and Use Committee of Fuzong Clinical College of Fujian Medical University.

## 2.3. Preparation of ATO/PpIX NPs

ATO/PpIX NPs were prepared by the self-assembly method (Hu et al., 2020). The prescription was further optimized using the central composite design. A three-factor, five-level, and alpha of 1.682 were chosen in Supplementary Table S1. And the data of central composite design were shown in Supplementary Table S2. The feeding molar ratio of ATO: PpIX (A), PpIX:TPGS (B), and prescription quality of PVP-K30 (C) as independent variables, and the overall desirability (OD) as the dependent variable were analyzed using Design-Expert 8.0.5 software. The optimal prescription was as follows: ATO (652  $\mu$ g), PpIX (250  $\mu$ g), TPGS (335  $\mu$ g) and PVP-K30 (10 mg) were mixed in 250  $\mu$ L of DMF, then added to 10 mL of ultrapure water. After stirring for 1 h, ATO/PpIX NPs were obtained and purified to remove free drugs and DMF by Amicon®Ultra-15 centrifuge tube (MWCO 100 kDa) with ultrapure water for five cycles. Similarly, cholesterol (CHOL) replaced ATO to prepare CHOL/PpIX NPs.

## 2.4. The characteristics of ATO/PpIX NPs

The morphology of nanoparticle was characterized by transmission electron microscopy (TEM). The size and zeta potential of nanoparticle were characterized by dynamic laser scattering (DLS, Litesizer 500, Austria). Physical phase states of ATO and PpIX in ATO/PpIX NPs were identified by X-ray diffraction (XRD) and differential scanning calorimetry (DSC). The drugs (ATO and PpIX) encapsulation efficiency (EE) or loading efficiency (DLE) by HPLC were calculated according to equation: EE = quality of drug loaded in ATO/PpIX NPs/quality of the initial drugs input  $\times$  100 %. DLE = quality of drug loaded in ATO/PpIX NPs/quality of ATO/PpIX NPs  $\times$  100 %.

The laser stability of PpIX in nanoparticle solutions was evaluated by laser irradiation. The absorbance values at 635 nm of free PpIX, ATO/PpIX NPs and CHOL/PpIX NPs solutions were investigated with 635 nm laser with a intensity of 300 mW/cm<sup>2</sup> for 60 min.

## 2.5. In vitro release behavior of ATO/PpIX NPs

The ATO cumulative release behavior of ATO/PpIX NPs was measured by dialysis. Briefly, 500  $\mu$ L of deproteinized ATO/PpIX NPs (ATO dose of 500  $\mu$ g/mL) was added to a dialysis bag (MWCO 100 kDa), and the dialysis bag was then immersed in 20 mL of PBS (pH 7.4, 6.5, 5.0) containing 0.5 % (v/v) tween 80. The solution were placed in a thermostatic incubation shaker (shaker) set at 37 °C for 100 rpm, and 200  $\mu$ L of release solution was collected at 0, 2, 4, 8, 12, 24, and 48 h, respectively, and supplemented with an same volume of release medium. The cumulative release rate of ATO was calculated by HPLC.

## 2.6. Hemolysis experiment of ATO/PpIX NPs

Blood was taken from a New Zealand rabbit ear margin vein, fibrinogen was removed and diluted with saline to prepare a 2 %

erythrocyte suspension. Add 750  $\mu$ L of ATO/PpIX NPs solution (PpIX dose of 1, 2.5, 5, 10, 20, 40  $\mu$ g/mL), saline (negative control), and purified water (positive control) to 625  $\mu$ L of 2 % erythrocyte suspension. Set up a group of sample solution without 2 % erythrocyte suspension. The tubes were gently shaken and incubated at 37 °C for 3 h, and 200  $\mu$ L of the supernatant was removed on a 96-well plate, and the absorbance was detected at 540 nm. The formula for calculating the hemolysis rate was as follows: where the absorbance of  $A_{sample}$  (sample),  $A_{100}$  (negative control), and  $A_0$  (positive control) were represented, respectively.

$$\text{Hemolysis}(\%) = \frac{A_{\text{sample}} - A_0}{A_{100} - A_0} \times 100\%$$

## 2.7. Cellular uptake assay

CT-26 cellular uptake of drugs were detected by confocal laser scanning microscopy (CLSM, SP5, Leica, USA) and flow cytometry (FACSVerse, BD, US). CT-26 cells ( $1 \times 10^6$  cells/well) were seeded into laser confocal glass-dishes or 6-well plates overnight. Subsequently, free PpIX and ATO/PpIX NPs were respectively added to each dish and incubated for different times (2, 4, and 6 h). Cells were washed with PBS, stained with DAPI, and then observed using CLSM. Alternatively, after washing in PBS, cells were digested with trypsin and detected by flow cytometry.

## 2.8. In vitro cytotoxicity and viable/dead measurement

CT-26 cells ( $1 \times 10^4$  cells/well) were cultured into 96-well plates overnight. The original medium was replaced with fresh medium containing different formulations and incubated for 48 h, followed by the MTT assay. The absorbance of each well was detected at 450 nm to represent the dark toxicity of the formulations.

The photodynamic cytotoxicity of ATO/PpIX NPs was also detected by the MTT assay. CT-26 cells with the same cell density as dark toxicity were inoculated in 96-well plates overnight. Fresh medium containing different formulations instead of the original medium. After 6 h of incubation, the cells were irradiated using the 635 nm laser (10 mW/cm<sup>2</sup>, 10 min). Subsequently, the cells were cultured for another 42 h and detected by the MTT assay. And the combination index (CI) of drug was determined by Compusyn software. Meanwhile, Calcein-AM/PI Staining Kit was used for staining the viable/dead cells. The CT-26 cells ( $1 \times 10^6$  cells/well) were cultured with different formulations in 6-well plates. The experiment was divided into 4 groups, which were PBS, ATO/PpIX NPs, CHOL/PpIX NPs plus Laser, and ATO/PpIX NPs plus Laser. The laser groups were irradiated using the 635 nm laser (10 mW/cm<sup>2</sup>, 10 min), and the final concentration was 1  $\mu$ mol/L (PpIX) and 3  $\mu$ mol/L (ATO), respectively. The staining procedure was carried out according to the manufacturer's instructions. Finally, the fluorescence was detected using fluorescent microscope.

## 2.9. In vitro ROS measurement

The intracellular ROS was measured using fluorescent microscope by DCFH-DA (Solarbio; China) as the probe. CT-26 cells ( $1 \times 10^5$  cells/well) were seeded into 6-well plates overnight. Subsequently, the CT-26 cells were cultured with ATO/PpIX NPs (ATO dose of 3  $\mu$ mol/L, PpIX dose of 1  $\mu$ mol/L) and CHOL/PpIX NPs (1  $\mu$ mol/L) for 6 h. The cells were then cleaned with PBS and interfered with DCFH-DA. For the laser group, the cells were irradiated by 635 nm laser (10 mW/cm<sup>2</sup>, 10 min). Finally, the ROS production of cells was detected by fluorescent microscope.

## 2.10. Dissolved oxygen measurement

CT-26 cells were treated with ATO/PpIX NPs, free ATO, and CHOL/PpIX NPs for 12 h, the dose of ATO and PpIX were 30  $\mu$ mol/L and 10  $\mu$ mol/L, respectively. The dissolved oxygen meter probe was inserted

under the liquid surface and sealed with a liquid paraffin to avoid gas exchange between the medium and the outside environment. After the reading have stabilized, recorded the change in dissolved oxygen (DO) in the medium for 1 h. The initial measurement value was 100 % and the relative oxygen content was calculated using the formula:

$$DO(\%) = \frac{DO_t}{DO_0} \times 100\%$$

### 2.11. Induced ICD with ATO/PpIX NPs

For CRT detection, CT-26 cells ( $1 \times 10^5$  cells/well) were seeded into laser confocal glass-dishes and cultured overnight. After 6 h incubation with different formulations (CHOL/PpIX NPs or ATO/PpIX NPs) under hypoxic condition, the laser group were irradiated by the 635 nm laser ( $10 \text{ mW/cm}^2$ , 10 min), and ATO dose of  $3 \mu\text{mol/L}$  or PpIX dose of  $1 \mu\text{mol/L}$  was set, respectively. After washing the cells with PBS, the cells were stained with Alexa Fluor 488-CRT (Beijing Biosynthesis; China) for 1 h and observed using CLSM.

For ATP detection, CT-26 cells ( $1 \times 10^6$  cells/well) were seeded into culture flasks (surface area of  $25 \text{ cm}^2$ ) overnight. After incubation with different formulations (CHOL/PpIX NPs or ATO/PpIX NPs) for 6 h under hypoxic condition, the laser group were irradiated using the 635 nm laser ( $10 \text{ mW/cm}^2$ , 10 min), and the dose of ATO or PpIX was the same as that of CRT group. Subsequently, intracellular ATP was measured using ATP content assay kit (Solarbio; China) according to the manufacturer's protocol.

Intracellular HMGB1 was determined by HMGB1 ELISA kit (Wuhan Huamei; China). Briefly, CT-26 cells were seeded into 96-well plates ( $1 \times 10^4$  cells/well) and treated with ATO/PpIX NPs and CHOL/PpIX NPs. After incubation for 6 h under hypoxic condition, the laser groups were irradiated using the 635 nm laser ( $10 \text{ mW/cm}^2$ , 10 min). Finally, intracellular HMGB1 was detected according to the manufacturer's instruction.

### 2.12. Biodistribution of nanoparticles in vivo

To investigate the distribution of nanoparticles *in vivo* and determine the time point of laser irradiation, CT-26 tumor-bearing mice (the tumor volume about  $100 \text{ mm}^3$ ) were injected intravenously with CHOL/PpIX NPs and ATO/PpIX NPs, and the dose of PpIX was  $5.1 \text{ mg/kg}$ . Briefly, At a predetermined time point, the mice were photographed using the IVIS Spectrum CT Imaging System (PerkinElmer, Inc. USA). After 24 h, major organs and tumor tissues were obtained and imaged.

### 2.13. Immunohistochemistry assay

CT-26 tumor-bearing xenografts were divided into 4 groups, which was intravenously injected with saline, ATO, CHOL/PpIX NPs and ATO/PpIX NPs solutions with the dose of ATO ( $10 \text{ mg/kg}$ ) and PpIX ( $5.1 \text{ mg/kg}$ ) once every 2 days for 4 times. Finally, tumor tissues were removed at the end of the treatment, and the expression of PD-L1 protein (1:200 dilution of PD-L1 antibody) was detected by immunohistochemistry.

### 2.14. Immune response analysis

CT-26 tumor-bearing xenografts were randomly divided into six groups ( $n = 3$ ). Such as: (1) saline; (2) anti-PD-L1; (3) ATO/PpIX NPs plus laser; (4) ATO/PpIX NPs coupled with anti-PD-L1; (5) CHOL/PpIX NPs plus laser coupled with anti-PD-L1; (6) ATO/PpIX NPs plus laser coupled with anti-PD-L1. On the 0, 2nd, 4th, and 6th day, CT-26 tumor-bearing mice were intravenously injected with ATO/PpIX NPs or CHOL/PpIX NPs (the dose of ATO and PpIX was  $10 \text{ mg/kg}$  or  $5.1 \text{ mg/kg}$ , respectively) and intraperitoneally injected with anti-PD-L1 ( $10 \text{ mg/kg}$ ). At 6 h post-injection, the mice in laser groups were irradiated using the 635 nm laser ( $300 \text{ mW/cm}^2$ , 10 min). 48 h after the last dose, the blood

samples were collected for the determination of blood biochemical indicators, and tumors or inguinal lymph nodes were removed for subsequent experiments.

Single-cell suspensions of inguinal lymph nodes were prepared by mechanical dissociation and stained with mixed antibodies. Mature DCs (MHC-II<sup>+</sup>CD11c<sup>+</sup>CD80<sup>+</sup>CD86<sup>+</sup>) were counted by flow cytometry.

For detecting the proportion of M1-type or M2-type TAMs, single-cell suspensions of tumor tissue were collected using the Mouse Tumor Dissociation Kit (Miltenyi Biotec; Germany), and single-cell suspensions were then stained with fluorescently-labeled flow antibodies. M1-type TAMs (CD11b<sup>+</sup>F4/80<sup>+</sup>CD11c<sup>+</sup>) and M2-type TAMs (CD11b<sup>+</sup>F4/80<sup>+</sup>CD206<sup>+</sup>) were measured by flow cytometry. The cytokines (TNF- $\alpha$ , IFN- $\gamma$ , IL-12, IL-6, and IL-10) were measured by a cytometric bead array (CBA) kit (BD, USA).

Tumor-infiltrating T cells were detected by immunofluorescence. The tumor tissue sections were stained with CD8 antibody (1:200), and Foxp3 antibody (1:100), followed by the addition of the responding fluorescent secondary antibody. Subsequently, fluorescence microscopy was used to observe and photographed to assess immune cell changes.

### 2.15. In vivo anti-CT-26-tumor evaluation

CT-26 cells were injected into the right armpit of mice to establish primary colon tumor model, which were randomly divided into six groups ( $n = 6$ ). The tumor-bearing mice of primary colon experiments were divided into same groups, administered dose and further treated as described in Section 2.14. The tumor volume was calculated by  $V = (\text{tumor length}) \times (\text{tumor width})^2/2$ . And relative tumor volume was defined as  $V/V_0$ , in which  $V_0$  represented the initiated volume before treatment. After 20 days, the tumor-bearing mice were executed to remove the tumors, photographed and weighed. Subsequently, the tumors from different groups were sliced for H&E staining to evaluate the tumor suppressive effect of the combined strategy.

### 2.16. In vivo anti-pulmonary metastatic effect

$1 \times 10^6$  4T1 cells/100  $\mu\text{L}$  were subcutaneously injected into the right armpit of mice, and the volume of tumor achieved about  $50\text{--}100 \text{ mm}^3$ , mice were randomly divided into six groups ( $n = 9$ ), the divided groups and drug administration regimen as described same in Section 2.14, which were given medicine on the 0, 2nd, 4th, and 6th day. After day 15, the tumor-bearing mice were injected with  $1 \times 10^5$  4T1 cells in the tail vein to establish a lung metastatic tumor model. Three mice in each group were killed on day 16 to obtain spleens to analyse for memory T cells. Effector memory T cells ( $T_{EM}$ ) (CD45<sup>+</sup>CD3<sup>+</sup>CD8<sup>+</sup>CD44<sup>+</sup>CD62L<sup>-</sup>) were counted by flow cytometry. The other mice were killed on day 30. Subsequently, the number of pulmonary nodules were recorded, and the nodules of tumor in the lung were examined by H&E staining.

### 2.17. Statistical analysis

One-way ANOVA was performed using GraphPad Prism software to identify significant differences between the groups. \* $p < 0.05$ , \*\* $p < 0.01$ , and \*\*\* $p < 0.001$  were indicated significant differences.

## 3. Results and discussion

### 3.1. Preparation and characterization of ATO/PpIX NPs

Oxygen relieving agent of ATO, photosensitizer of PpIX, and stabilizers of PVP-K30 together with TPGS were selected for the preparation of self-delivery photodynamic-hypoxia alleviating nanomedicine (ATO/PpIX NPs). The nanoparticles formed by self-assembly have high drug loading efficiency and simple preparation process (Venditto and Szoka, 2013). The structures of ATO and PpIX determine their high probability of self-assembly (Fu et al., 2021; Shi et al., 2022), while the feeding

ratios of ATO and PpIX needed to be optimized. After the preliminary investigation of a single-factor, the prescription and process were further optimized using central composite design. The feeding molar ratio of ATO:PpIX (A) or PpIX:TPGS (B), and prescription quality of PVP-K30 (C) were used as independent variables, ranging from A (3:1–5:1), B (1:1–3:1), and C (10–30 mg). The encapsulation efficiency and average size of the nanoparticles were converted into an overall desirability (OD) to obtain the optimal prescription. 3D response surfaces and 2D contour plots of the independent and dependent OD variables were plotted using Design-Expert 8.0.5 software (Fig. 1A and Fig. S1). Obviously, at the feeding molar ratio of ATO:PpIX (4:1), PpIX:TPGS (1:2) and quality of PVP-K30 (10 mg), the optimal prescription of ATO/PpIX NPs were obtained. And the DLE for PpIX and ATO in the optimal prescription was calculated to be 22.3 % and 46.5 %. Besides, the morphology of ATO/PpIX NPs was nanorod-like particles (Fig. 1B), which can be determined by the combination of the nature of the drug itself and interaction forces (Zhao et al., 2020). The planar PpIX molecules were stacked in an arrangement, which may provide a site for the growth of ATO, or encounter ATO due to an attractive interaction. The size (130.2 nm), PDI (0.12) and zeta potential (-20.1 mV) of the ATO/PpIX NPs were measured by the DLS. The carboxyl group carried in PpIX may be dissociated and therefore negatively charged. Subsequently, the UV absorption spectra of free PpIX, CHOL/PpIX NPs and ATO/PpIX NPs with the 635 nm laser irradiation (300 mW/cm<sup>2</sup>, 60 min) and absorbance at 635 nm were shown in Fig. 1C and Supplementary Table S3. The nanoparticles group (CHOL/PpIX NPs and ATO/PpIX NPs) under laser irradiation degraded <15 % within 10 min and about 20 % within 60 min, indicating that after the formation of nanoparticles, the

photostability was improved. In contrast, free PpIX was already degraded about 25 % within 10 min, and the drug degradation reached about 35 % within 60 min, indicating the poor photostability of the free photosensitizer. Photostability also demonstrated that laser irradiation intensity (300 mW/cm<sup>2</sup>, 10 min) did not lead to significant degradation of the photosensitizer in animal experiments.

Whether the physical phase of the drug (ATO and PpIX) changed after self-assembly to form nanoparticles. As shown in Fig. 1D, the characteristic absorption diffraction peaks of ATO and PpIX were evident in the range of 17 °C–27 °C by the XRD, indicating that both ATO and PpIX existed in microcrystalline state, while the peaks of ATO and PpIX were significantly lower in ATO/PpIX NPs, suggesting that ATO or PpIX may exist in nanoparticles in microcrystalline and amorphous forms. The same results were determined by DSC. The characteristic absorption peaks of ATO and PpIX appeared at 222 °C and 198 °C respectively, and could also be found in the physical mixture by the DSC. In contrast, the characteristic absorption peak of ATO/PpIX NPs was clearly “blue-shifted” and weakened, however the characteristic absorption peak of the drug was still visible, indicating that ATO or PpIX may be present in a mixture of microcrystalline and amorphous forms in the nanoparticles (Fig. 1E).

The release of nanoparticles in the tumor microenvironment (TME) is the key to anti-tumor effect (Wen et al., 2022). The release behavior of nanoparticles at different pH was investigated to explore the TME responsiveness of nanoparticles. As shown in Fig. 1F, the cumulative release of ATO was only (35.21 ± 2.61)% at pH 7.4, whereas reached (39.77 ± 2.50)% or (45.89 ± 3.62)% at pH 6.5 or 5.0 respectively. ATO and PpIX self-assembled into nanoparticles with hydrophobic

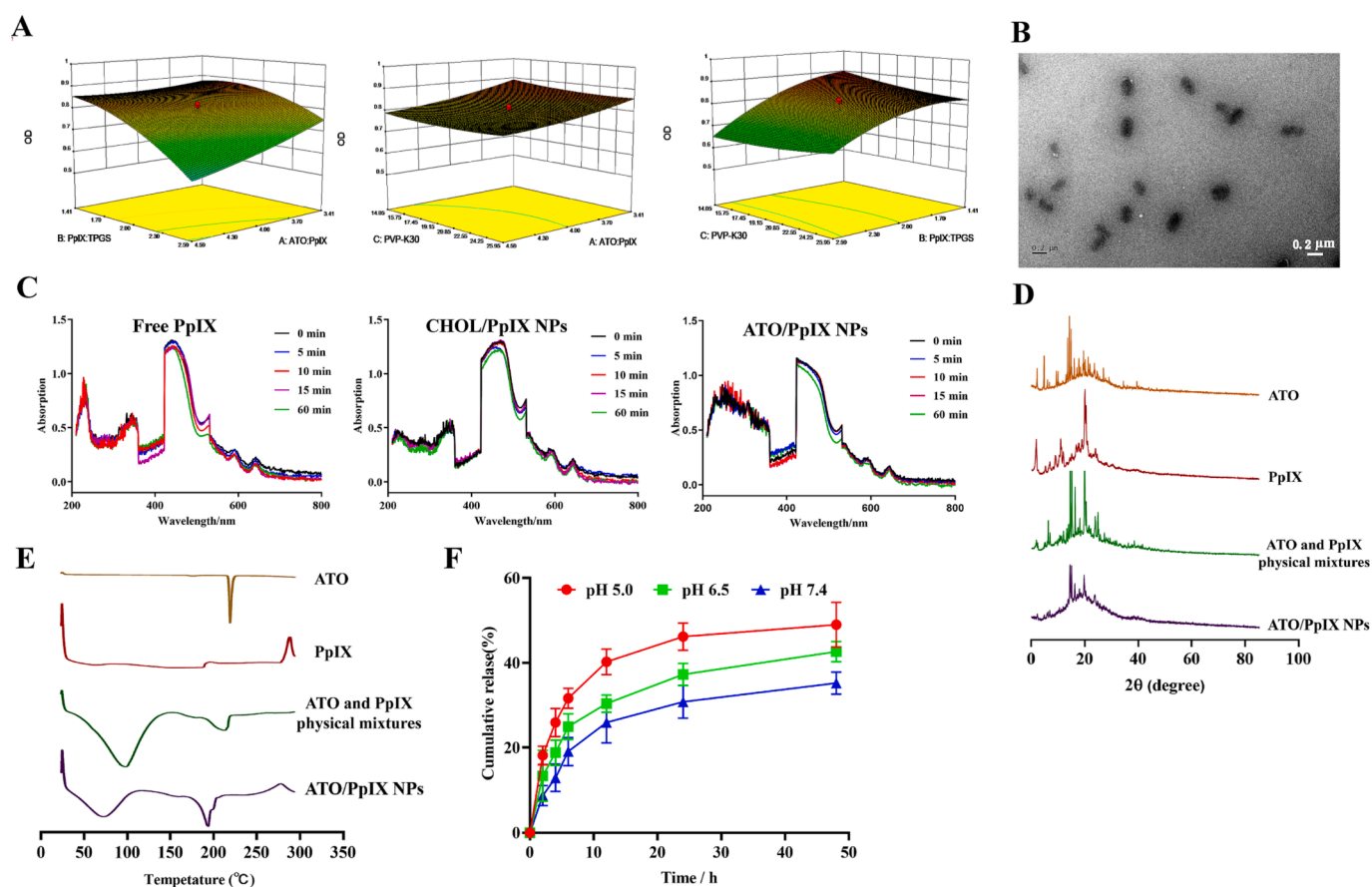


**Fig. 1.** Nanoparticle characterization. (A) The 3D response surfaces were plotted using Design-Expert 8.0.5 software. (B) The morphology of ATO/PpIX NPs was identified by TEM. (C) Evaluation of laser irradiation stability of different formulations with 635 nm laser (300 mW/cm<sup>2</sup>). (D) X-ray diffraction patterns and (E) differential scanning calorimetry of ATO, PpIX, ATO/PpIX NPs, physical mixture of ATO, PpIX, TPGS and PVP-K30. (F) *In vitro* release of ATO from ATO/PpIX NPs with pH 7.4, 6.5, 5.0, n = 3.



improved hypoxia-enhanced PDT.

### 3.3. O<sub>2</sub>-economized PDT induced ICD evaluation *in vitro*

Oxygen can flow in and out of the cell membrane by free diffusion. Schematic illustration was shown in Fig. 3A, oxygen consumption of tumor cells was measured indirectly by measuring changes in oxygen content of the culture medium after isolation of the external environment by liquid paraffin. Compared to PBS or CHOL/PpIX NPs group, oxygen consumption was decreased significantly in the ATO or ATO/PpIX NPs groups (Fig. 3B). The result indicated that ATO could reduce cellular oxygen consumption, which is beneficial for the subsequent PDT-induced ICD and alleviating hypoxic microenvironment.

There are various ways to activate the host immune system, such as the use of adjuvants, ICD triggers, etc (Ren et al., 2021; Zhao et al., 2022). Damaged-associated molecular patterns are released during the ICD cascade, which induce the maturation of antigen-presenting cells and then activate the host immune system (Li et al., 2022a). CRT can be found outside of the cytoplasm to release the “eat me” signal. As shown in Fig. 3C, the massive CRT exposure of ATO/PpIX NPs plus laser irradiation was observed by CLSM, which displayed strong green fluorescence outside of the cytoplasm. The green fluorescence of CHOL/PpIX NPs plus laser group slightly lower than ATO/PpIX NPs plus laser group, while higher than no laser irradiation group. The released ATP can act as a “find me” signal to present the tumor antigen, and released HMGB1 from intracellular to extracellular can induce the maturation of antigen presenting cell (Zhang et al., 2022; Zhou et al., 2021). Subsequently, intracellular ATP and HMGB1 were observed by kit. As shown in Fig. 3D and 3E, decreased intracellular of ATP and HMGB1 levels were observed with ATO/PpIX NPs plus laser irradiation, implying that ATO/PpIX NPs plus laser irradiation can effectively modulate the release of ATP and HMGB1 through the synergistic effect of ATO to improve hypoxia and thus enhance the efficacy of PDT-mediated ICD. The less intracellular ATP and HMGB1 mean more are released extracellularly, indicating a

higher degree of ICD. The above results suggested that ATO/PpIX NPs plus laser irradiation was expected to synergistically enhance photodynamically induced ICD by improving tumor hypoxia, laying the foundation for subsequent proposals to activate the host immune system.

### 3.4. Biodistribution of ATO/PpIX NPs *in vivo*

Prior to anti-tumor pharmacodynamic experiments *in vivo*, it was necessary to explore the biodistribution of nanoparticles on CT-26 tumor-bearing mice to determine the time point of laser irradiation and the enrichment of nanoparticles in tumor tissue. As shown in Fig. 4A, the tumor-bearing mice were intravenously injected with nanoparticle solutions (CHOL/PpIX NPs or ATO/PpIX NPs), and the fluorescence signals of PpIX on the tumor site progressively enriched and reached highest point at about 6 h after the injection, and then gradually decreased. This indicated that the EPR effect of nanoparticles contributed to massive accumulation in tumor tissue. After 24 h, the isolated fluorescence images of the main organs and tumor confirmed the effective enrichment of nanoparticles in the tumor tissues and the nanoparticles were metabolized through the liver (Fig. 4B). The point at 6 h was selected as the laser irradiation time to explore the efficacy and mechanism of PDT.

### 3.5. Therapeutic efficacy on CT-26 primary tumor *in vivo*

Inspired by excellent ICD *in vitro* and the substantial tumor accumulation of the ATO/PpIX NPs *in vivo*, we then assessed the therapeutic potential of anti-CT-26 primary tumors. The six groups of tumor-bearing mice were set to saline, anti-PD-L1, ATO/PpIX NPs plus laser, ATO/PpIX NPs coupled with anti-PD-L1, CHOL/PpIX NPs plus laser coupled with anti-PD-L1, and ATO/PpIX NPs plus laser coupled with anti-PD-L1. As shown in Fig. 5A, CT-26 tumor-bearing xenografts were intravenously injected with nanoparticle solutions, treated with laser irradiation 6 h post-injection and injected intraperitoneally with anti-PD-L1

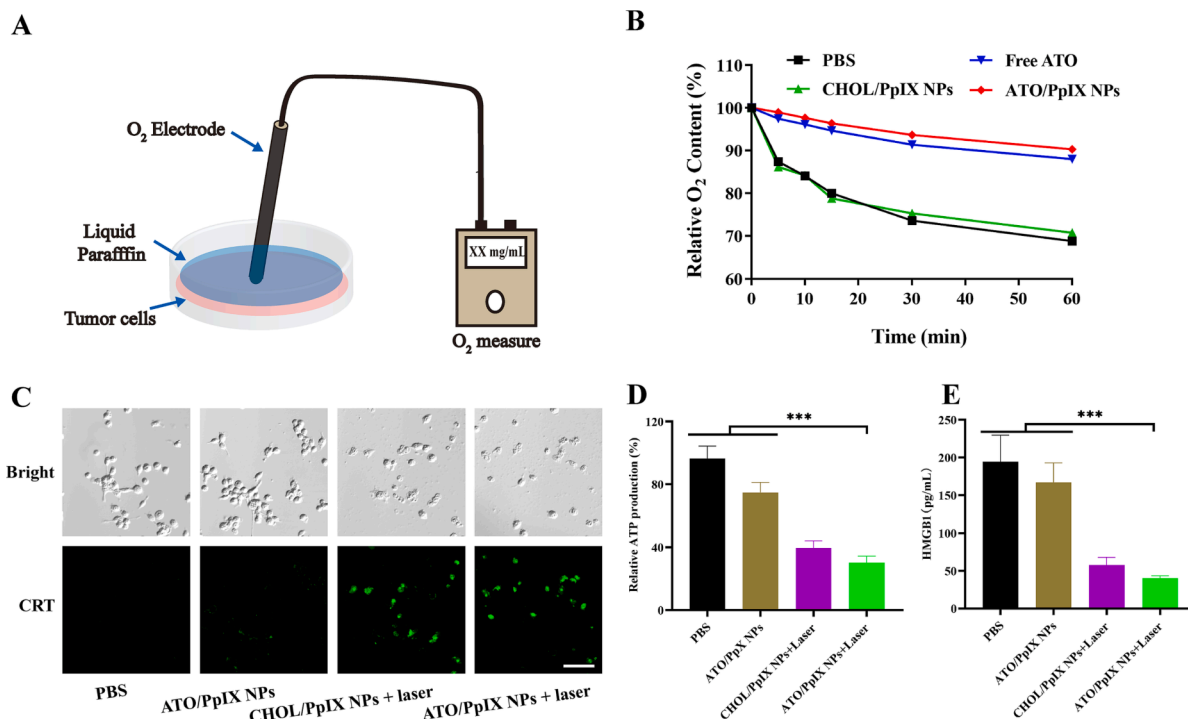
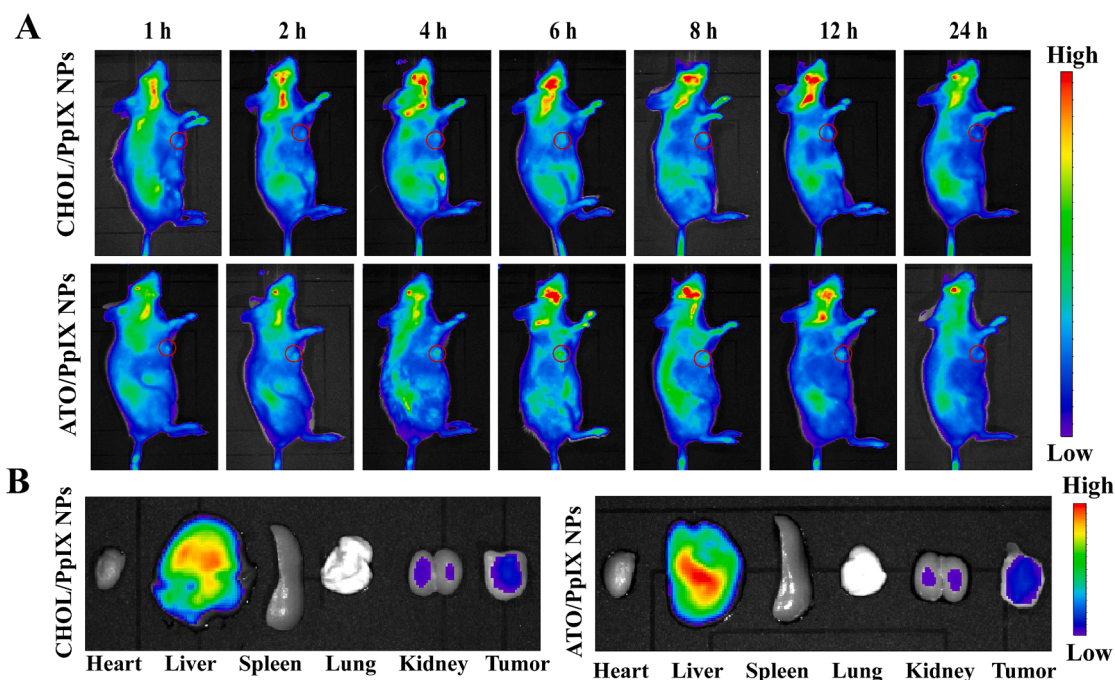


Fig. 3. O<sub>2</sub>-economized nanoparticle-induced ICD evaluation. (A) Schematic illustration of the oxygen consumption of CT-26 cells in the medium measured by dissolved oxygen meter. (B) Relative oxygen concentration of CT-26 cells in the medium after different formulations was determined by dissolved oxygen meter. (C) CRT expression in CT-26 cells after different drugs with laser or no laser irradiation, scale bars: 20  $\mu$ m. (D) Determination of intracellular ATP concentration by ATP content assay kit, n = 3. (E) Intracellular HMGB1 content determined by HMGB1 ELISA kit, n = 3. Data represent mean  $\pm$  SD.



**Fig. 4.** Biodistribution of nanoparticles assay. (A) *In vivo* fluorescence distribution of nanoparticles at different time points in the tumor-bearing mice. (B) *In vitro* fluorescence distribution of nanoparticles in main organs and tumor tissue after 24 h. Data represent mean  $\pm$  SD.

monoclonal antibody on the 0, 2nd, 4th, and 6th day. The mice's weight and tumor volumes were observed every 2 days. The mice's weight showed a decreasing trend during the treatment, possibly due to fix the limbs during the trial, which affected the status of mice. However, the mice's weight continued to gain at the end of the drug treatments (Fig. 5B). As shown in Fig. 5C and 5D, anti-PD-L1 group exhibited a slight tumor-suppressive effect compared with the saline group. In contrast, ATO/PpIX NPs plus laser or ATO/PpIX NPs coupled with anti-PD-L1 groups exhibited the partly tumor-suppressive effect, which were attributed to improved oxygen enhancing PDT or improved tumor hypoxic immunosuppressive microenvironment to activate the host immune system. Besides, CHOL/PpIX NPs plus laser coupled with anti-PD-L1 group was inferior to ATO/PpIX NPs plus laser coupled with anti-PD-L1 group (Fig. 5E and 5F). This was attributed to alleviate hypoxia to enhance PDT while also improve the hypoxic immunosuppressive microenvironment, which in turn promoted anti-tumor immunotherapy. Furthermore, H&E staining is a common method to examine tumor tissue for apoptosis and damage. Compared to the other groups, the ATO/PpIX NPs plus laser coupled with anti-PD-L1 group showed damaged cytoplasm, loss of nuclear atrophy and extensive damage (Fig. 5G). All these results demonstrated that photodynamic-alleviating hypoxic-immunotherapy could show a strong, synergistic anti-tumor therapeutic effectiveness.

### 3.6. ATO/PpIX NPs plus laser coupled with anti-PD-L1 stimulated the host immune system

Accordance with the excellent anti-CT-26 primary tumor efficacy, the potential mechanism that photodynamic-alleviating hypoxic-immunotherapy mediated anti-tumor immune response was investigated *in vivo*. It is well known that only a small number of cancer patients are sensitive to PD-1/PD-L1 immune checkpoint inhibitors (ICIs), most likely due to the low expression of PD-L1, low immunogenicity, and hypoxic immunosuppressive microenvironment (Élez et al., 2022; Kong et al., 2019; Zheng et al., 2022). The NCCN Oncology Clinical Practice Guidelines states that patient's tumor PD-L1 biomarker status should be evaluated to determine their applicability to ICIs therapy (Benson et al., 2022). Firstly, PD-L1 expression in different groups of tumor sections

was detected by immunohistochemistry after the drugs intervention. As shown in Fig. S3, PD-L1 protein expression was low in the saline or ATO/PpIX NPs without laser groups, and significantly increased in the CHOL/PpIX NPs plus laser or ATO/PpIX NPs plus laser groups, suggesting that photodynamic therapy could induce upregulation of PD-L1 expression in tumor samples, which was consistent with published article (Yuan et al., 2021). The increased expression of PD-L1 in tumor acts like a "double-edged sword", and although high expression of PD-L1 inhibits the function of cytotoxic T lymphocytes, the current studies show that high PD-L1 expression is positively correlated with tumor response with ICIs (Tong et al., 2022). Next, ICD-based DCs ( $CD80^+CD86^+$ , gated from  $MHC-II^+CD11c^+$ ) in lymph nodes was further explored. The ATO/PpIX NPs plus laser coupled with anti-PD-L1 group had a higher proportion of mature DCs than that of saline group, indicating a synergistic effect of the strategy to recombine the immunosuppressive TME (Fig. 6A). Thus, the release of tumor-associated antigens to promote DCs maturation during the PDT-induced ICD could enhance tumor immunogenicity and potentially stimulate T cell activation, which further highlighting the potential of PDT-mediated DC maturation. Subsequently, we continued to explore whether improved hypoxia induces tumor-associated macrophage (TAM) polarization. *In vitro* dissolved oxygen experiments showed that ATO significantly reduced cellular oxygen consumption (Fig. 3B), which may potentially lead to M2-type TAMs polarization to M1-type TAMs in TME. M1-type TAMs ( $CD11c^+$ , gated from  $CD11b^+F4/80^+$ ) percentage in tumors of ATO/PpIX NPs plus laser coupled with anti-PD-L1 group (41.1 %) was higher than saline (15.4 %), anti-PD-L1 (17.8 %), CHOL/PpIX NPs plus laser coupled with anti-PD-L1 (22.9 %), ATO/PpIX NPs plus laser (29.8 %), and ATO/PpIX NPs coupled with anti-PD-L1 groups (32.0 %) (Fig. 6B, 6C and Fig. S4). Compared to the saline group, a distinctly lower M2-type TAMs ( $CD206^+$ , gated from  $CD11b^+F4/80^+$ ) were discovered among ATO/PpIX NPs plus laser coupled with anti-PD-L1 group. The results of the change in TAMs phenotype were consistent with the previous literature (Huang et al., 2022). The polarization of TAMs could lead to changes in pro-inflammatory and anti-inflammatory factors and potentially enhance T cell immune function. Thus a series of cytokines including pro-inflammatory (TNF- $\alpha$ , IFN- $\gamma$ , and IL-12) and anti-inflammatory (IL-10, and IL-4) in tumor tissues were detected using a cytometric bead array

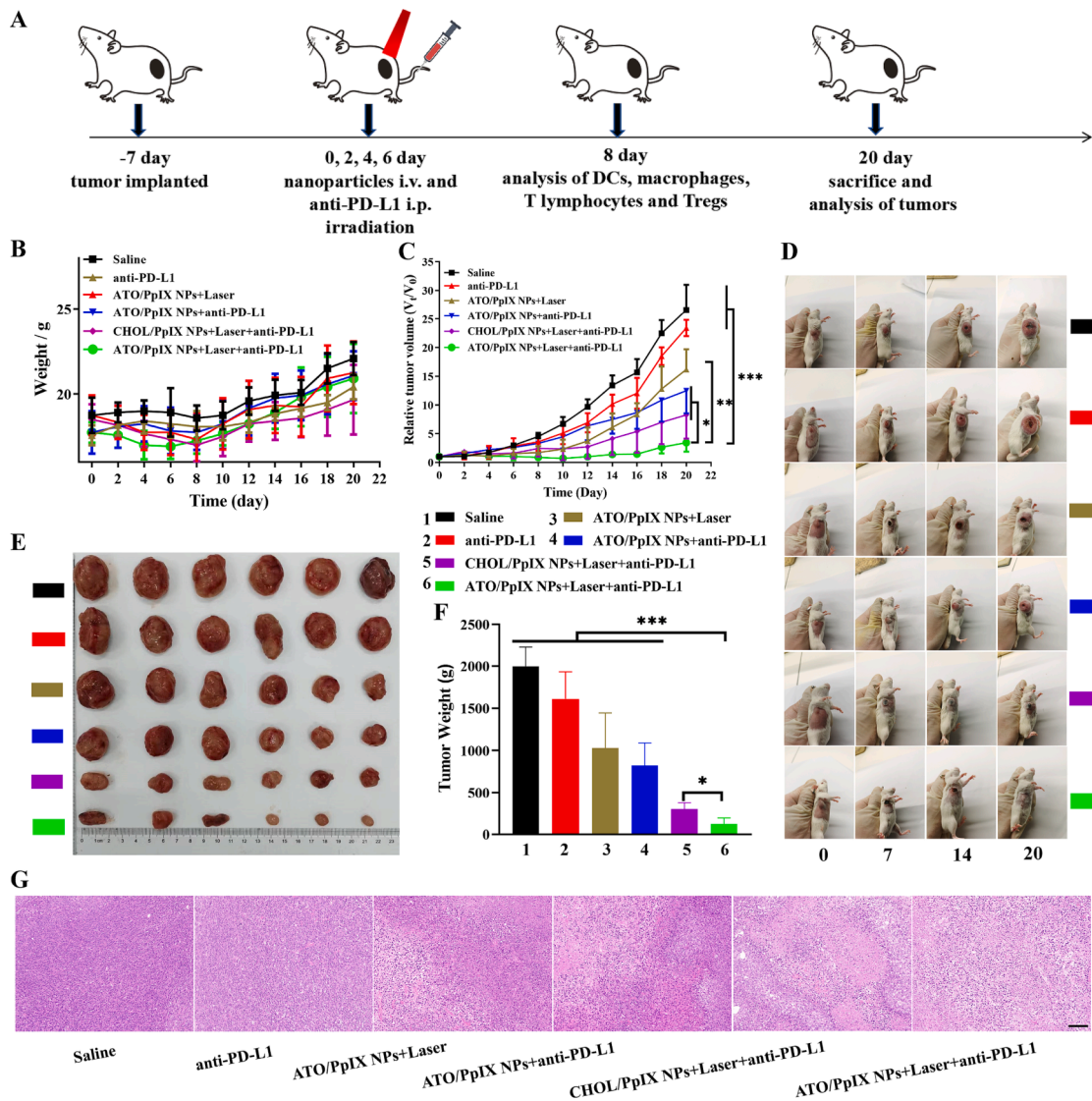


**Fig. 5.** Evaluation of inhibition effect of CT-26 primary tumor. (A) Schematic illustration of the anti-CT-26 primary tumor experimental design. (B) Curves of mice's body weight changes in each group, n = 6. (C) Relative tumor volume changes of different groups from CT-26 tumor-bearing mice, n = 6. (D) Representative images of CT-26-bearing mice on different days. (E) *In vitro* images and (F) weights of CT-26 tumors on the 20th day, n = 6. (G) H&E stained images of CT-26 tumors from different groups, scale bar: 100  $\mu$ m. Data represent mean  $\pm$  SD.

(CBA) kit by flow cytometry. As shown in Fig. 6D, 6E and 6F, TNF- $\alpha$ , IFN- $\gamma$ , and IL-12 were elevated in ATO/PpIX NPs plus laser coupled with anti-PD-L1 group compared with the saline group. And the decreased IL-10 or IL-4 level in tumor tissues were found for ATO/PpIX NPs plus laser coupled with anti-PD-L1 group (Fig. 6G and 6H), suggesting that combined strategy could activate the pro-inflammatory responses and reduce anti-inflammatory effects. Characterization of "cold" in the TME, including upregulation of Tregs and downregulation of cytotoxic T cells (Vanneman and Dranoff, 2012; Zhu et al., 2022). Finally, immunofluorescence was used to determine changes in T cell types in tumor sections after the treatments. As shown in Fig. 6I, The massive infiltration of CD8<sup>+</sup>T lymphocytes in ATO/PpIX NPs plus laser coupled with anti-PD-L1 group was investigated, implying that the reversal from "cold" to "hot" in TME may enhance the anti-tumor efficacy. In addition, compared to the saline group, immunosuppressive Tregs (Foxp3<sup>+</sup>) were observably reduced in ATO/PpIX NPs plus laser coupled with anti-PD-L1 group. These results were attributed to photodynamic induction of ICD-promoted dendritic cell maturation, macrophage polarization induced by alleviating hypoxia, and blockade of the PD-1/PD-L1 pathway by PD-L1 monoclonal antibodies, which were synergistic stimulation of T cell-

mediated immune responses.

### 3.7. *In vivo anti-pulmonary metastatic tumor evaluation*

Malignant tumors are aggressive, systemic spread and prone to metastasis, which is responsible for clinical treatment failure (Hossain et al., 2021). Inspired by the prominent role of photodynamic-alleviating hypoxic-immunotherapy in suppressing CT-26 primary tumors, we further challenged to treat the whole-body metastatic tumor model. Compared to CT-26 tumor model, the 4T1 tumor model is more invasive and systemic spread (Derakhshan and Reis-Filho, 2022). Thus we further estimated the curative effect of ATO/PpIX NPs plus laser coupled with anti-PD-L1 in 4T1 pulmonary metastatic tumor. The mice were intravenously injected with 4T1 cells ( $1 \times 10^5$ ) on day 15 after the drug treatments, and the spleens of the tumor-bearing mice were taken for detection of the effector memory T cells (T<sub>EM</sub> cells) on day 16, and the remaining mice fed until the end of the experiment, lung tissues were taken for metastasis analysis (Fig. 7A). As indicated in Fig. 7B and 7C, the number of lung metastatic nodules of saline group and anti-PD-L1 group were maximum, which were greatly reduced in ATO/PpIX NPs

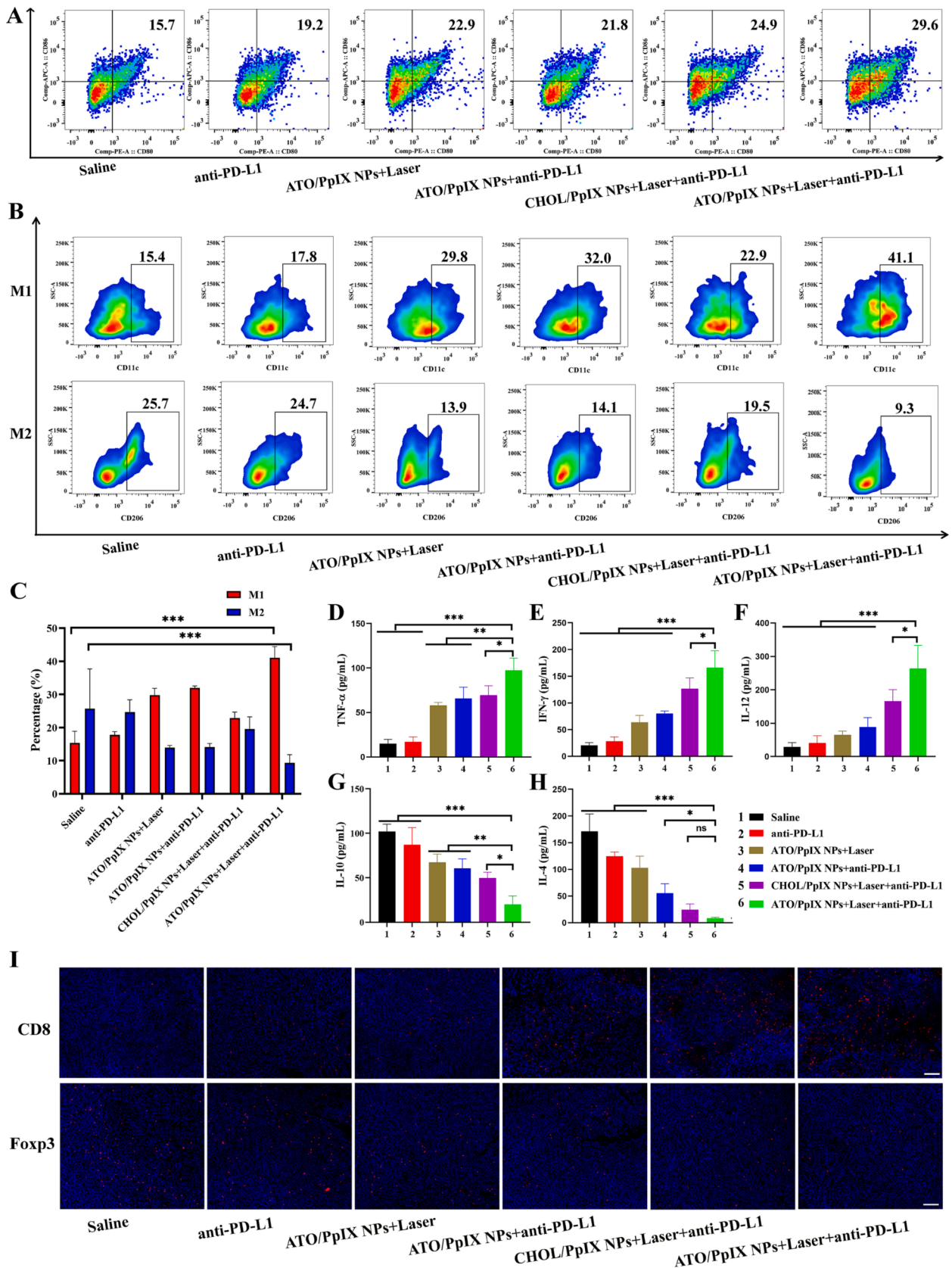


**Fig. 6.** Evaluation of anti-tumor immune response by ATO/PpIX NPs plus laser coupled with PD-L1 blockade. (A) The proportions and flow cytometry plots of mature dendritic cells in lymph nodes from different groups. (B) The proportions and (C) quantitative flow results of M1-type TAMs and M2-type TAMs,  $n = 3$ . The expression levels of TNF- $\alpha$  (D), IFN- $\gamma$  (E), IL-12 (F), IL-10 (G), and IL-4 (H) were detected using a cytometric bead array (CBA) kit by flow cytometry in different groups,  $n = 3$ . (I) Representative immunofluorescence images of CD8<sup>+</sup> and Foxp3<sup>+</sup> in the CT-26 tumor-bearing mice from different groups, scale bar: 100  $\mu$ m. Data represent mean  $\pm$  SD.

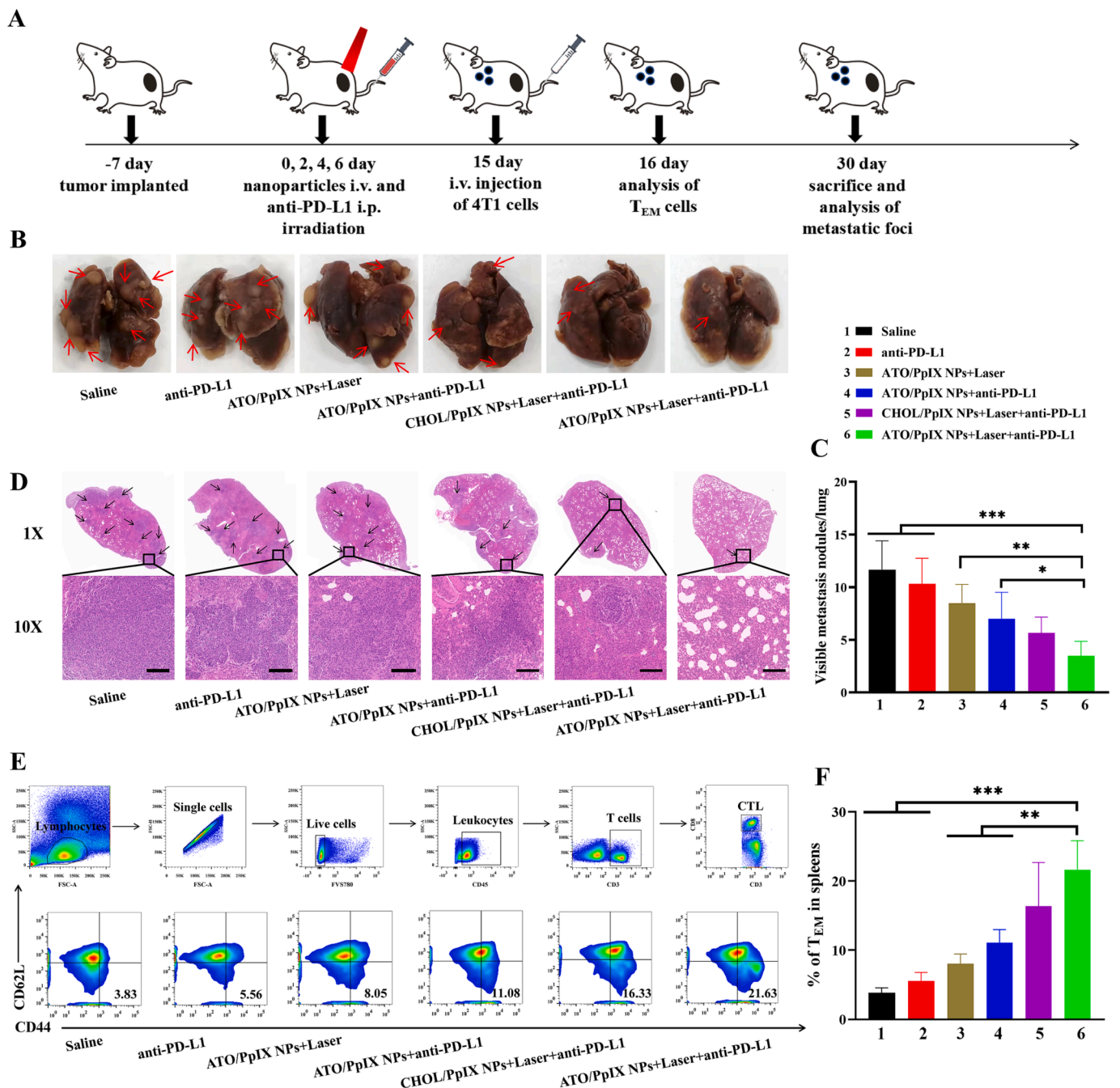


**Fig. 7.** Evaluation of inhibition effect of pulmonary metastasis on 4T1 tumor. (A) Schematic illustration of the tumor metastasis experimental design. (B) Representative images of tumor metastasis and (C) quantitative metastasis nodules from the lung tissues, n = 6. (D) Representative images of H&E staining from lung tissues, scale bars: 100 μm. (E) Representative images and (F) quantitative T<sub>EM</sub> cells in the spleens were detected by flow cytometry from different groups (gated on CD45<sup>+</sup>CD3<sup>+</sup>CD8<sup>+</sup>CD44<sup>+</sup>CD62L<sup>-</sup>), n = 3. Data represent mean ± SD.

plus laser coupled with anti-PD-L1 group. In addition, as the H&E staining shown in Fig. 7D, the infiltrating 4T1-tumor cells in the lungs treated with saline were massive, while remarkable inhibition of ATO/PpIX NPs plus laser coupled with anti-PD-L1 group were measured. The results indicated that ATO/PpIX NPs plus laser coupled with anti-PD-L1 mediated photodynamic-alleviating hypoxic-immunotherapy could active immune response against metastatic 4T1 tumors.

As we know, T<sub>EM</sub> cells could induce immediate protection by producing cytokines, which play an important role in long-term immune memory against tumors (Abou-Daya et al., 2021). The potential to produce a long-term immune response is a significant feature of the immune systems. Therefore, to better explore the underlying mechanism

of adaptive immunity establishment against metastatic 4T1 tumors, we analyzed the T<sub>EM</sub> cells in the spleens using flow cytometry. The percentage of T<sub>EM</sub> cells (CD45<sup>+</sup>CD3<sup>+</sup>CD8<sup>+</sup>CD44<sup>+</sup>CD62L<sup>-</sup>) from the ATO/PpIX NPs plus laser coupled with anti-PD-L1 groups was much higher than that of the other groups (Fig. 7E and 7F), indicating that the photodynamic-alleviating hypoxia together with PD-1/PD-L1 blockade could induce a long-term immune memory effect and effectively prevent tumor metastasis.

### 3.8. The safety evaluation

The safety of formulations is a major concern prior to the clinical

application of anti-neoplastic therapy (Wicki et al., 2015). The blood biocompatibility of the drug was evaluated by a hemolysis test, which could provide the basis for intravenous administration. Hemolysis occurred in the positive control tube (purified water) and was absent in the negative control tube (saline) (Fig. S5 A). And the hemolysis rate of nanoparticle solutions remained below 5 % at high concentration (40 µg/mL), suggesting that ATO/PpIX NPs had good blood biocompatibility (Fig. S5 B). ALT and AST can reflect the damage of liver function, BUN and CRE are the main indicators reflecting the function of kidney, and CK exists in the myocardium, which is one of the indicators of whether the heart is impaired. There was no significant difference in ALT, AST, BUN, CRE and CK in each drug treatment group compared to the saline group ( $p > 0.05$ ) (Fig. S6). All these results confirmed that the strategy of nanopatform mediated therapy had no significant toxic side effects and was excellent biocompatibility *in vivo*.

#### 4. Conclusion

In summary, self-assembled rationally engineered ATO/PpIX NPs plus laser coupled with anti-PD-L1 that contemporaneously improved low immunogenicity, severe hypoxia, and immunosuppressive TME could serve on valid O<sub>2</sub>-economized PDT-induced ICD stimulants, M1-type TAMs polarizing reactor, and PD-L1 blocker. Firstly, improved hypoxia by ATO could enhance PDT-induced ICD and promote DCs maturation, which stimulated the systemic immune response. Meanwhile, the improvement of the hypoxic microenvironment could induce M2-type TAMs polarization to M1-type TAMs, which effectively enhanced T-cell activation. Moreover, anti-PD-L1 could enhance T-cell function by blocking the PD-1/PD-L1 pathway. Therefore, the promising conjugation strategy could inhibit CT-26 primary colon tumor and 4T1 pulmonary metastatic breast cancer by stimulating systemic immune response, which may provide photodynamic-alleviating hypoxic-immunotherapy against cancers.

#### CRedit authorship contribution statement

**Xianquan Feng:** Conceptualization, Writing – original draft, Formal analysis, Methodology, Visualization. **Zhenzhen Chen:** Conceptualization, Visualization, Methodology, Resources. **Zhihong Liu:** Funding acquisition, Resources. **Xiaoling Fu:** Methodology, Resources. **Hongtao Song:** Conceptualization, Project administration, Supervision, Funding acquisition, Visualization, Writing – review & editing. **Qian Zhang:** Conceptualization, Methodology, Investigation, Visualization, Funding acquisition.

#### Declaration of Competing Interest

The authors declare that they have no known competing financial interests or personal relationships that could have appeared to influence the work reported in this paper.

#### Data availability

Data will be made available on request.

#### Acknowledgments

This research was supported by the Natural Science Foundation of Fujian Province (Grant number: 2022J01491, 2021J01690). We would like to thank Junjin Lin, Shuping Zheng from the Public Technology Service Center (Fujian Medical University, Fuzhou, China) for technical support.

#### Appendix A. Supplementary material

Supplementary data to this article can be found online at <https://doi.org/10.1016/j.ijpharm.2023.122970>.

[org/10.1016/j.ijpharm.2023.122970](https://doi.org/10.1016/j.ijpharm.2023.122970).

#### References

- Aaes, T.L., Vandenabeele, P., 2021. The intrinsic immunogenic properties of cancer cell lines, immunogenic cell death, and how these influence host antitumor immune responses. *Cell Death Differ.* 28 (3), 843–860. <https://doi.org/10.1038/s41418-020-00658-y>.
- Abou-Data, K.I., Tieu, R., Zhao, D., Rammal, R., Sacirbegovic, F., Williams, A.L., Shlomchik, W.D., Oberbarnscheidt, M.H., Lakkis, F.G., 2021. Resident memory T cells form during persistent antigen exposure leading to allograft rejection. *Sci. Immunol.* 6 (57), eabc8122. <https://doi.org/10.1126/sciimmunol.abc8122>.
- Anderson, K.G., Stromnes, I.M., Greenberg, P.D., 2017. Obstacles posed by the tumor microenvironment to T cell activity: a case for synergistic therapies. *Cancer Cell* 31 (3), 311–325. <https://doi.org/10.1016/j.ccell.2017.02.008>.
- Ashton, T.M., Fokas, E., Kunz-Schughart, L.A., Folkes, L.K., Anbalagan, S., Huether, M., Kelly, C.J., Pirovano, G., Buffa, F.M., Hammond, E.M., Stratford, M., Muschel, R.J., Higgins, G.S., McKenna, W.G., 2016. The anti-malarial atovaquone increases radiosensitivity by alleviating tumour hypoxia. *Nat. Commun.* 7, 12308. <https://doi.org/10.1038/ncomms12308>.
- Bai, R., Li, Y., Jian, L., Yang, Y., Zhao, L., Wei, M., 2022. The hypoxia-driven crosstalk between tumor and tumor-associated macrophages: mechanisms and clinical treatment strategies. *Mol. Cancer* 21 (1), 177. <https://doi.org/10.1186/s12943-022-01645-2>.
- Benson, A.B., Venook, A.P., Al-Hawary, M.M., Azad, N., Chen, Y.-J., Ciombor, K.K., Cohen, S., Cooper, H.S., Deming, D., Garrido-Laguna, I., Grem, J.L., Gunn, A., Hecht, J.R., Hoffe, S., Hubbard, J., Hunt, S., Jeck, W., Johung, K.L., Kirilcuk, N., Krishnamurthi, S., Maratt, J.K., Messersmith, W.A., Meyerhardt, J., Miller, E.D., Mulcahy, M.F., Nurkin, S., Overman, M.J., Parikh, A., Patel, H., Pedersen, K., Saltz, L., Schneider, C., Shibata, D., Skibber, J.M., Sofocleous, C.T., Stotsky-Himelfarb, E., Tavakkoli, A., Willett, C.G., Gregory, K., Gurski, L., 2022. Rectal Cancer, Version 2.2022, NCCN Clinical Practice Guidelines in Oncology. *J. Natl. Compr. Cancer Netw. JNCCN* 20 (10), 1139–1167. <https://doi.org/10.6004/jnccn.2022.0051>.
- Choi, J., Sun, I.-C., Sook Hwang, H., Yeol Yoon, H., Kim, K., 2022. Light-triggered photodynamic nanomedicines for overcoming localized therapeutic efficacy in cancer treatment. *Adv. Drug Deliv. Rev.* 186, 114344. <https://doi.org/10.1016/j.addr.2022.114344>.
- Derakhshan, F., Reis-Filho, J.S., 2022. Pathogenesis of triple-negative breast cancer. *Annu. Rev. Pathol.* 17, 181–204. <https://doi.org/10.1146/annurev-pathol-042420-093238>.
- Élez, E., Mulet-Margalef, N., Sanso, M., Ruiz-Pace, F., Mancuso, F.M., Comas, R., Ros, J., Argilés, G., Martini, G., Sanz-García, E., Baraibar, I., Salvà, F., Noguerido, A., Cuadrá-Urteaga, J.L., Fasani, R., García, A., Jimenez, J., Aguilar, S., Landolfi, S., Hernández-Losa, J., Brana, I., Nuciforo, P., Dienstmann, R., Taberno, J., Salazar, R., Vivancos, A., 2022. A comprehensive biomarker analysis of microsatellite unstable/mismatch repair deficient colorectal cancer cohort treated with immunotherapy. *Int. J. Mol. Sci.* 24 (1), 118. <https://doi.org/10.3390/ijms24010118>.
- Fu, S., Li, G., Zhang, W., Zhou, X., Shi, K., Zhai, Y., 2021. Pure drug nano-assemblies: a facile carrier-free nanopatform for efficient cancer therapy. *Acta Pharm. Sin. B* 12 (1), 92–106. <https://doi.org/10.1016/j.apsb.2021.08.012>.
- Gao, W., Zhang, J., Wang, W., Liu, Z., Chen, M., Hu, X., Zeng, L., Zheng, C., Song, H., Zhang, Q., 2022. Drug self-delivery nanorods enhance photodynamic therapy of triple-negative breast cancer by inhibiting oxidative phosphorylation. *Int. J. Pharm.* 621, 121775. <https://doi.org/10.1016/j.ijpharm.2022.121775>.
- Griffiths, G., Gruenberg, J., Marsh, M., Wohlmann, J., Jones, A.T., Parton, R.G., 2022. Nanoparticle entry into cells; the cell biology weak link. *Adv. Drug Deliv. Rev.* 188, 114403. <https://doi.org/10.1016/j.addr.2022.114403>.
- He, G., Li, Y., Younis, M.R., Fu, L.-H., He, T., Lei, S., Lin, J., Huang, P., 2022. Synthetic biology-instructed transdermal microneedle patch for traceable photodynamic therapy. *Nat. Commun.* 13 (1), 6238. <https://doi.org/10.1038/s41467-022-33837-1>.
- Hossain, F., Majumder, S., David, J., Miele, L., 2021. Precision medicine and triple-negative breast cancer: current landscape and future directions. *Cancers* 13 (15), 3739. <https://doi.org/10.3390/cancers13153739>.
- Hu, S., Dong, C., Wang, J., Liu, K., Zhou, Q., Xiang, J., Zhou, Z., Liu, F., Shen, Y., 2020. Assemblies of indocyanine green and chemotherapeutic drug to cure established tumors by synergistic chemo-photo therapy. *J. Control. Release* 324, 250–259. <https://doi.org/10.1016/j.jconrel.2020.05.018>.
- Huang, M., Xiong, D., Pan, J., Zhang, Q., Wang, Y., Myers, C.R., Johnson, B.D., Hardy, M., Kalyanaraman, B., You, M., 2022. Prevention of tumor growth and dissemination *in situ* vaccination with mitochondria-targeted atovaquone. *Adv. Sci.* 9 (12), e2101267. <https://doi.org/10.1002/adv.202101267>.
- Im, B.N., Shin, H., Lim, B., Lee, J., Kim, K.S., Park, J.M., Na, K., 2021. Helicobacter pylori-targeting multiligand photosensitizer for effective antibacterial endoscopic photodynamic therapy. *Biomaterials* 271, 120745. <https://doi.org/10.1016/j.biomaterials.2021.120745>.
- Jiao, X., Sun, L., Zhang, W., Ren, J., Zhang, L., Cao, Y., Xu, Z., Kang, Y., Xue, P., 2021. Engineering oxygen-deficient ZrO nanopatform as therapy-activated “immunogenic cell death (ICD)” inducer to synergize photothermal-augmented sonodynamic tumor elimination in NIR-II biological window. *Biomaterials* 272, 120787. <https://doi.org/10.1016/j.biomaterials.2021.120787>.
- Kong, P., Wang, J., Song, Z., Liu, S., He, W., Jiang, C., Xie, Q., Yang, L., Xia, X., Xia, L., 2019. Circulating lymphocytes, PD-L1 expression on tumor-infiltrating lymphocytes,

- and survival of colorectal cancer patients with different mismatch repair gene status. *J. Cancer* 10 (7), 1745–1754. <https://doi.org/10.7150/jca.25187>.
- Lai, C., Luo, B., Shen, J., Shao, J., 2022. Biomedical engineered nanomaterials to alleviate tumor hypoxia for enhanced photodynamic therapy. *Pharmacol. Res.* 186, 106551. <https://doi.org/10.1016/j.phrs.2022.106551>.
- Le, Y., Gao, H., Bleday, R., Zhu, Z., 2018. The homeobox protein VentX reverts immune suppression in the tumor microenvironment. *Nat. Commun.* 9 (1), 2175. <https://doi.org/10.1038/s41467-018-04567-0>.
- Li, J.-Y., Chen, Y.-P., Li, Y.-Q., Liu, N., Ma, J., 2021a. Chemotherapeutic and targeted agents can modulate the tumor microenvironment and increase the efficacy of immune checkpoint blockades. *Mol. Cancer* 20 (1), 27. <https://doi.org/10.1186/s12943-021-01317-7>.
- Li, Z., Lai, X., Fu, S., Ren, L., Cai, H., Zhang, H., Gu, Z., Ma, X., Luo, K., 2022b. Immunogenic cell death activates the tumor immune microenvironment to boost the immunotherapy efficiency. *Adv. Sci. (Weinh.)* 9, e2201734. <https://doi.org/10.1002/advs.202201734>.
- Li, Y., Liu, X., Zhang, X., Pan, W., Li, N., Tang, B., 2021b. Immunogenic cell death inducers for enhanced cancer immunotherapy. *Chem. Commun. (Camb.)* 57 (91), 12087–12097. <https://doi.org/10.1039/d1cc04604g>.
- Li, L., Tian, H., Zhang, Z., Ding, N., He, K., Lu, S., Liu, R., Wu, P., Wang, Y., He, B., Luo, M., Peng, P., Yang, M., Nice, E.C., Huang, C., Xie, N., Wang, D., Gao, W., 2022a. Carrier-free nanoplatform via evoking pyroptosis and immune response against breast cancer. *ACS Appl. Mater. Interfaces* 15 (1), 452–468. <https://doi.org/10.1021/acsami.2c17579>.
- Liao, C., Liu, X., Zhang, C., Zhang, Q., 2023. Tumor hypoxia: from basic knowledge to therapeutic implications. *Semin. Cancer Biol.* 88, 172–186. <https://doi.org/10.1016/j.semcancer.2022.12.011>.
- Ren, X., Wang, N., Zhou, Y., Song, A., Jin, G., Li, Z., Luan, Y., 2021. An injectable hydrogel using an immunomodulating gelator for amplified tumor immunotherapy by blocking the arginase pathway. *Acta Biomater.* 124, 179–190. <https://doi.org/10.1016/j.actbio.2021.01.041>.
- Rodell, C.B., Arlauckas, S.P., Cuccarese, M.F., Garris, C.S., Li, R., Ahmed, M.S., Kohler, R. H., Pittet, M.J., Weissleder, R., 2018. TLR7/8-agonist-loaded nanoparticles promote the polarization of tumour-associated macrophages to enhance cancer immunotherapy. *Nat. Biomed. Eng.* 2 (8), 578–588. <https://doi.org/10.1038/s41551-018-0236-8>.
- Ruffell, B., Coussens, L.M., 2015. Macrophages and therapeutic resistance in cancer. *Cancer Cell* 27 (4), 462–472. <https://doi.org/10.1016/j.ccell.2015.02.015>.
- Scharping, N.E., Menk, A.V., Whetstone, R.D., Zeng, X., Delgoffe, G.M., 2017. Efficacy of PD-1 blockade is potentiated by metformin-induced reduction of tumor hypoxia. *Cancer Immunol. Res.* 5 (1), 9–16. <https://doi.org/10.1158/2326-6066.CCR-16-0103>.
- Secomb, T.W., Hsu, R., Ong, E.T., Gross, J.F., Dewhirst, M.W., 1995. Analysis of the effects of oxygen supply and demand on hypoxic fraction in tumors. *Acta Oncol. (Stockholm, Sweden)* 34 (3), 313–316. <https://doi.org/10.3109/02841869509093981>.
- Shahpour, M., Adili-Aghdam, M.A., Mahmudi, H., Jaymand, M., Amoozgar, Z., Akbari, M., Hamblin, M.R., Jahanban-Esfahlan, R., 2022. Prospects for hypoxia-based drug delivery platforms for the elimination of advanced metastatic tumors: from 3D modeling to clinical concepts. *J. Control. Release* 353, 1002–1022. <https://doi.org/10.1016/j.jconrel.2022.12.009>.
- Shi, J., Nie, W., Zhao, X., Yang, X., Cheng, H., Zhou, T., Zhang, Y., Zhang, K., Liu, J., 2022. Intracellular self-assembly driven uninterrupted ROS generator augments 5-aminolevulinic acid-based tumor therapy. *Adv. Mater.* 34 (30), e2201049. <https://doi.org/10.1002/adma.202201049>.
- Tong, Q., Xu, J., Wu, A., Zhang, C., Yang, A., Zhang, S., Lin, H., Lu, W., 2022. Pheophorbide A-mediated photodynamic therapy potentiates checkpoint blockade therapy of tumor with low PD-L1 expression. *Pharmaceutics* 14 (11), 2513. <https://doi.org/10.3390/pharmaceutics14112513>.
- Vanneman, M., Dranoff, G., 2012. Combining immunotherapy and targeted therapies in cancer treatment. *Nat. Rev. Cancer* 12 (4), 237–251. <https://doi.org/10.1038/nrc3237>.
- Venditto, V.J., Szoka Jr., F.C., 2013. Cancer nanomedicines: so many papers and so few drugs! *Adv. Drug Deliv. Rev.* 65 (1), 80–88. <https://doi.org/10.1016/j.addr.2012.09.038>.
- Villacampa, G., Tolosa, P., Salvador, F., Sánchez-Bayona, R., Villanueva, L., Dienstmann, R., Ciruelos, E., Pascual, T., 2022. Addition of immune checkpoint inhibitors to chemotherapy versus chemotherapy alone in first-line metastatic triple-negative breast cancer: a systematic review and meta-analysis. *Cancer Treat. Rev.* 104, 102352. <https://doi.org/10.1016/j.ctrv.2022.102352>.
- Wen, Y.-H., Hsieh, P.-I., Chiu, H.-C., Chiang, C.-W., Lo, C.-L., Chiang, Y.-T., 2022. Precise delivery of doxorubicin and imiquimod through pH-responsive tumor microenvironment-active targeting micelles for chemo- and immunotherapy. *Mater Today Bio* 17, 100482. <https://doi.org/10.1016/j.mtbio.2022.100482>.
- Wicki, A., Witzigmann, D., Balasubramanian, V., Huwyler, J., 2015. Nanomedicine in cancer therapy: challenges, opportunities, and clinical applications. *J. Control. Release* 200, 138–157. <https://doi.org/10.1016/j.jconrel.2014.12.030>.
- Xia, C., Dong, X., Li, H., Cao, M., Sun, D., He, S., Yang, F., Yan, X., Zhang, S., Li, N., Chen, W., 2022. Cancer statistics in China and United States, 2022: profiles, trends, and determinants. *Chin Med J (Engl)* 135 (5), 584–590. <https://doi.org/10.1097/CM9.00000000000002108>.
- Yang, Z., Gao, D., Guo, X., Jin, L., Zheng, J., Wang, Y., Chen, S., Zheng, X., Zeng, L., Guo, M., Zhang, X., Tian, Z., 2020. Fighting immune cold and reprogramming immunosuppressive tumor microenvironment with red blood cell membrane-camouflaged nanobullets. *ACS Nano* 14 (12), 17442–17457. <https://doi.org/10.1021/acsnano.0c07721>.
- Yang, M., Zhang, C., Wang, R., Wu, X., Li, H., Yoon, J., 2023. Cancer immunotherapy elicited by immunogenic cell death based on smart nanomaterials. *Small Methods* e2201381. <https://doi.org/10.1002/smt.202201381>.
- Yuan, Z., Fan, G., Wu, H., Liu, C., Zhan, Y., Qiu, Y., Shou, C., Gao, F., Zhang, J., Yin, P., 2021. Photodynamic therapy synergizes with PD-L1 checkpoint blockade for immunotherapy of CRC by multifunctional nanoparticles. *Mol. Ther.* 29 (10), 2931–2948. <https://doi.org/10.1016/j.ymthe.2021.05.017>.
- Zhang, J., Jiang, C., Figueiró Longo, J.P., Azevedo, R.B., Zhang, H., Muehlmann, L.A., 2018. An updated overview on the development of new photosensitizers for anticancer photodynamic therapy. *Acta Pharm. Sin. B* 8 (2), 137–146. <https://doi.org/10.1016/j.apsb.2017.09.003>.
- Zhang, M., Qin, X., Zhao, Z., Du, Q., Li, Q., Jiang, Y., Luan, Y., 2022. A self-amplifying nanodrug to manipulate the Janus-faced nature of ferroptosis for tumor therapy. *Nanoscale Horiz.* 7 (2), 198–210. <https://doi.org/10.1039/d1nh00506e>.
- Zhao, Z., Li, Q., Qin, X., Zhang, M., Du, Q., Luan, Y., 2022. An injectable hydrogel reshaping adenosinergic axis for cancer therapy. *Adv. Funct. Mater.* 32 (24), 2200801. <https://doi.org/10.1002/adfm.202200801>.
- Zhao, H., Zhao, B., Wu, L., Xiao, H., Ding, K., Zheng, C., Song, Q., Sun, L., Wang, L., Zhang, Z., 2019. Amplified cancer immunotherapy of a surface-engineered antigenic microparticle vaccine by synergistically modulating tumor microenvironment. *ACS Nano* 13 (11), 12553–12566. <https://doi.org/10.1021/acsnano.9b03288>.
- Zhao, L.-P., Zheng, R.-R., Huang, J.-Q., Chen, X.-Y., Deng, F.-A., Liu, Y.-B., Huang, C.-Y., Yu, X.-Y., Cheng, H., Li, S.-Y., 2020. Self-delivery photo-immune stimulators for photodynamic sensitized tumor immunotherapy. *ACS Nano* 14 (12), 17100–17113. <https://doi.org/10.1021/acsnano.0c06765>.
- Zheng, Z., Bian, C., Wang, H., Su, J., Meng, L., Xin, Y., Jiang, X., 2022. Prediction of immunotherapy efficacy and immunomodulatory role of hypoxia in colorectal cancer. *Ther. Adv. Med. Oncol.* 14, 17588359221138383. <https://doi.org/10.1177/17588359221138383>.
- Zhou, Y., Ren, X., Hou, Z., Wang, N., Jiang, Y., Luan, Y., 2021. Engineering a photosensitizer nanoplatform for amplified photodynamic immunotherapy via tumor microenvironment modulation. *Nanoscale Horiz.* 6 (2), 120–131. <https://doi.org/10.1039/d0nh00480d>.
- Zhu, L., Li, J., Guo, Z., Kwok, H.F., Zhao, Q., 2022. Synergistic combination of targeted nano-nuclear-reactors and anti-PD-L1 nanobodies evokes persistent T cell immune activation for cancer immunotherapy. *J. Nanobiotechnol.* 20 (1), 521. <https://doi.org/10.1186/s12951-022-01736-8>.